

Integrated Nano-Domains of Disordered and Ordered Spinel Phases in $\text{LiNi}_{0.5}\text{Mn}_{1.5}\text{O}_4$ for Li-Ion Batteries

Jung-Hyun Kim,^{*,†} Ashfia Huq,[‡] Miaofang Chi,[§] Nicholas P.W. Pieczonka,[⊥] Eunseok Lee,[#] Craig A. Bridges,^{||} Misle M. Tessema,[∇] Arumugam Manthiram,[○] Kristin A. Persson,[#] and Bob R. Powell[†]

[†]Chemical & Materials Systems Laboratory, General Motors Global R&D Center, Warren, Michigan 48090, United States

[‡]Spallation Neutron Source, [§]Center for Nanophase Materials Sciences, ^{||}Chemical Sciences Division, Oak Ridge National Laboratory, Oak Ridge, Tennessee 37831, United States

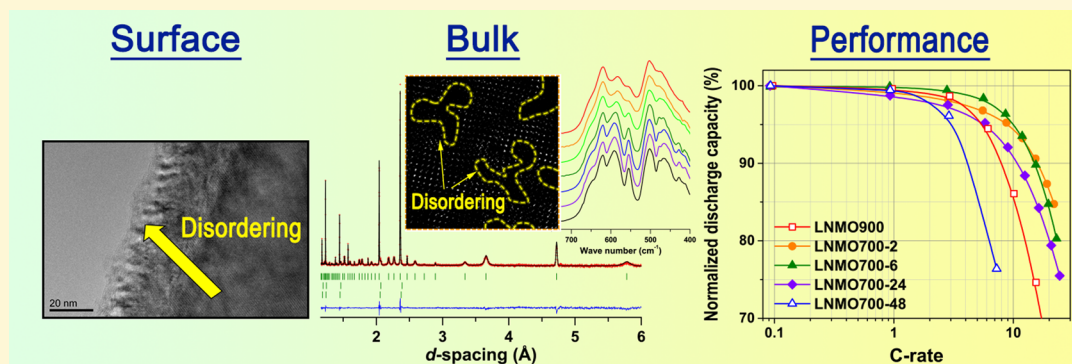
[⊥]Optimal CAE Inc., Plymouth, Michigan 48170, United States

[#]Environmental Energy Technologies Division, Lawrence Berkeley National Laboratory, Berkeley, California 94720, United States

[∇]Engineering Operations, GM Global Powertrain, Warren, Michigan 48090, United States

[○]Materials Science and Engineering Program, The University of Texas at Austin, Austin, Texas 78712, United States

Supporting Information



ABSTRACT: Recent calculations and experimental data suggest that understanding the local ordering behavior of Ni/Mn will be critical to optimize the electrochemical properties of $\text{LiNi}_{0.5}\text{Mn}_{1.5}\text{O}_4$ (LNMO) high voltage spinel. In this study, we systematically controlled the evolution of Ni and Mn ordering in LNMO samples by annealing them at 700 °C in air for different dwelling times, followed by quenching to room temperature. The long- and short-range ordering behavior of Ni and Mn were analyzed by combining neutron powder diffraction, X-ray powder diffraction (XRD), transmission electron microscopy (TEM), and Fourier transform infrared spectroscopy (FT-IR) data. The results show that the fraction of ordered phase increases rapidly during initial annealing at 700 °C for 6 h, and accompanied by decreasing amounts of secondary phases. Annealing longer than 6 h led to the growth in size of ordered domains (i.e., increased segregation of ordered and disordered domains) along with a slow increase in the fraction of ordered phase. The dependence of open circuit voltages (OCVs) of the LNMO on the degree of ordering agrees well with recent calculations using the density functional theory. The increase in the degree of ordering increases the open circuit voltage (OCV) and the initial capacity but reduces cycle life and rate capability. The LNMO delivered optimal battery performances (capacity, cycle life, and rate capability) after annealing at 700 °C for 2 h. This partially ordered sample showed the respective advantages from both disordered and ordered spinels: better spinel-phase purity (thus, higher initial capacity) from the ordered LNMO and better cycle life and rate capability from the disordered LNMO.

INTRODUCTION

LNMO spinel has attracted interest as a potential positive electrode material for Li-ion batteries.^{1–3} It is not only environmentally benign but provides good battery performance in terms of energy and power densities. For example, the $\text{Ni}^{2+/4+}$ redox in LNMO occurs at a relatively high voltage (ca. 4.7 V vs Li) compared with $\text{Ni}^{2+/4+}$ or $\text{Co}^{3+/4+}$ redox potentials in conventional layer-structure positive electrode materials such as LiCoO_2 or $\text{LiNi}_{1/3}\text{Co}_{1/3}\text{Mn}_{1/3}\text{O}_2$.⁴ The higher voltage increases the energy density of battery cells. LNMO also offers

significant enhancement in power capability because of rapid Li^+ ion transport via three-dimensional diffusion channels in the lattice.

The crystal structure and formation of rock-salt secondary phases in LNMO spinel has been actively investigated by several groups.^{5–9} LNMO crystallizes into two different

Received: April 4, 2014

Revised: June 22, 2014

Published: July 3, 2014

symmetries depending on the occurrence and degree of disordering/ordering of Ni²⁺ and Mn⁴⁺ in the lattice. The ordering between Ni and Mn (1:3 ratio) lowers the symmetry from $Fd\bar{3}m$ (disorder) to $P4_332$ (order); for example, Ni and Mn are disordered in octahedral interstitials (16d-site) for the $Fd\bar{3}m$ symmetry. Amatucci et al.^{9,10} systematically studied the effect of synthetic conditions (temperature and pO_2) on the crystal structure of the LNMO and found that the order-to-disorder transition occurred at higher temperatures (690–740 °C) with increasing pO_2 .

The disordering of LNMO is closely related with the formation of oxygen vacancies and the presence of a rock-salt phase. In the literature, the chemical composition of the rock-salt phase has been suggested to be $Li_{1-x}Ni_xO$, $(Li_xMn_{0.66}Ni_{0.34})_yO$, and/or Ni_6MnO_8 ; although the exact chemical composition has not been conclusively determined yet and may in fact vary with synthesis procedure, it is agreed that they are Ni-rich phases.^{6,7,11–13} Song et al.¹⁴ suggested that the rock-salt structure forms as a result of Mn (16d), Ni (16d), and/or Li (8a) diffusion into neighboring octahedral interstitial (16c) while maintaining face centered cubic array of oxygen ions at elevated temperatures (>700 °C). The rock-salt secondary phases again disappear once the disordered LNMO spinel (with oxygen vacancy) was annealed at 700 °C in air, indicating the reversible phase transition between spinel and rock-salt.

The effect of crystal structures on the electrochemical properties of LNMO has been investigated.^{5,6,9,10,14–16} The electrical conductivity of disordered LNMO showed 2.5 order of magnitude higher values than that of ordered LNMO, which can be explained by the higher electron conduction between mixed Mn^{3+/4+} cations compared with pure Mn⁴⁺.⁹ It was suggested that disordered LNMO has higher Li⁺ ion diffusion than the ordered phase.^{10,17} In addition, the ordered $Li_{1-x}Ni_xMn_{1.5}O_4$ experiences three-steps of phase transition in the range of $0 \leq x \leq 1$, while the disordered spinel only experiences two-steps of phase transition.^{5,15} As a result, the disordered LNMO demonstrated better rate performance and/or cycle life compared with the ordered LNMO. However, the formation of the rock-salt secondary phase is inevitable for the disordered LNMO because it requires heat-treatment at temperature higher than 800 °C. The rock-salt secondary phases were known to be electrochemically inactive.^{14,16} Therefore, the formation of the Ni-rich rock-salt secondary phase lowers the capacity and deviates the stoichiometry of the LNMO, which increases Mn³⁺ content and consequently lowers the energy density due to the relatively low redox voltage of Mn^{3+/4+} (~4 V vs Li). Recent TEM study showed that the rock-salt phase presents at the surface of LNMO particles,⁶ which may impede Li⁺ ion and electron transport.

It has been recently pointed out that LNMO may contain a significant amount of short-range Ni/Mn ordering rather than purely ordered or disordered phases. The short-range ordering strongly depends on cooling-rate after sintering at 900 °C because the cooling-rate will determine the amount of oxygen uptake for the LNMO at around 700 °C.^{14,16} For example, the electrochemical properties of the slow-cooled LNMO were more consistent with those of ordered LNMO as compared with fast-cooled LNMO. Shin et al. also reported a possible short-range ordering of Ni and Mn in the $LiNi_{0.5-x}M_xMn_{1.5}O_4$ ($M = Cr, Fe, \text{ and } Ga$).⁷ Their powder neutron diffraction study manifested angstrom-size ordered domains in $Li-$

$Ni_{0.5-x}M_xMn_{1.5}O_4$, as evidenced by broad reflections associated with Ni/Mn ordering.

To understand the structure-electrochemical property relationship in LNMO, several groups have performed computational simulations using first-principle energy calculations.^{18–21} A recent study by Lee et al.^{19,20} suggested that the lab-synthesized Ni/Mn ordered LNMO samples were not perfectly ordered based on the deviation of voltage profiles between simulated and experimental data. They calculated several phase diagrams of LNMO based on local structure changes, which agreed well with experimental data.^{5,22}

Recent calculations and experimental data suggest that understanding the local ordering behavior of Ni/Mn will be critical to optimize the electrochemical properties of LNMO. In this work, we systematically controlled the evolution of Ni and Mn ordering in LNMO samples by annealing them at 700 °C for different dwelling times, followed by quenching to room temperature. The 700 °C has been considered as an optimal temperature for the ordering of Ni/Mn.¹⁰ The evolution of ordered phase in the parent disordered LNMO spinel was monitored, and their impact on the electrochemical performance was investigated.

EXPERIMENTAL SECTION

Materials Preparation. LNMO powder sample was synthesized via solid-state reaction. Stoichiometric amounts of ⁷LiOH·H₂O (99.9%, Sigma-Aldrich), NiCO₃ (99%, Alfa Aesar), and MnCO₃ (99.985%, Alfa Aesar) precursors were mixed using a ball-mill (SPEX 8000D) for 30 min. The mixed precursors were pelletized and heated at 500 °C for 12 h in air. The resulting powders were reground, pelletized, and heated at 650 °C for 12 h in air. This synthesis was completed with a final heat treatment at 900 °C for 6 h in air. As expected, the resulting LNMO exhibited disordering between Ni and Mn.^{5,6} The Ni and Mn disordered LNMO was annealed at 700 °C in air for different times (0–48 h), followed by quenching to room-temperature. Table 1 lists the nomenclatures of the various samples investigated in this report.

Table 1. Nomenclatures of Samples Investigated

nomenclatures	sample descriptions
LNMO900	$LiNi_{0.5}Mn_{1.5}O_4$ (LNMO) synthesized at 900 °C
LNMO700-2	annealed the LNMO900 at 700 °C for 2 h in air
LNMO700-6	annealed the LNMO900 at 700 °C for 6 h in air
LNMO700-12	annealed the LNMO900 at 700 °C for 12 h in air
LNMO700-24	annealed the LNMO900 at 700 °C for 24 h in air
LNMO700-36	annealed the LNMO900 at 700 °C for 36 h in air
LNMO700-48	annealed the LNMO900 at 700 °C for 48 h in air

Material Characterization. The particle surfaces were further characterized using transmission electron microscopy (TEM). The TEM microscope was an aberration-corrected FEI Titan 60/300 kV. Powder X-ray diffraction (XRD) measurements were carried out with a Bruker D8 Advance Diffractometer with Cu $K\alpha_1$ radiation in Bragg–Brentano configuration. Powder neutron diffraction measurements were conducted at the POWGEN diffractometer (beamline 11A) at the Spallation Neutron Source at Oak Ridge National Laboratory. To suppress the neutron absorption from ⁶Li, a ⁷Li enriched precursor was used. The LNMO powder samples were analyzed via the Rietveld method using the GSAS/EXPGui and FullProf programs and with the ⁷Li scattering length.^{23–25} Data collected on LaB₆ were used as a resolution standard for application of the Scherrer equation. Fourier transform infrared spectroscopy (FT-IR) spectra were acquired with a Nicolet instrument with 2 cm⁻¹ resolution using KBr pellets containing 0.5 wt % LNMO.

Electrochemical Analysis. The LNMO positive electrode consisted of 80:10:10 wt % LNMO, super-P carbon, and polyvinylidene fluoride (PVDF, Kynar HSV 900), which were mixed with *N*-methylpyrrolidone (NMP) and coated onto an Al foil via the doctor-blade method. Coin half-cells (Hohsen Co. 2032 model) with lithium foil as the negative electrode were assembled in an argon-filled glovebox. Two layers of separator (Celgard, PP/PE/PP trilayer), and a 1 M LiPF₆ in ethylene carbonate (EC)/diethyl carbonate (DEC) (1/2 vol. ratio) electrolyte were used. All coin cells were cycled using a Maccor 4000 battery testing system. A Solartron potentiostat was used to record the open circuit voltages (OCV) of the Li_{1-x}Ni_{0.5}Mn_{1.5}O₄ half-cells after 6 h dwell at different states of charge (SOCs).

RESULTS AND DISCUSSION

TEM Analysis of LNMO Spinel. Parts a–d of Figure 1 show TEM images and selected area electron diffraction

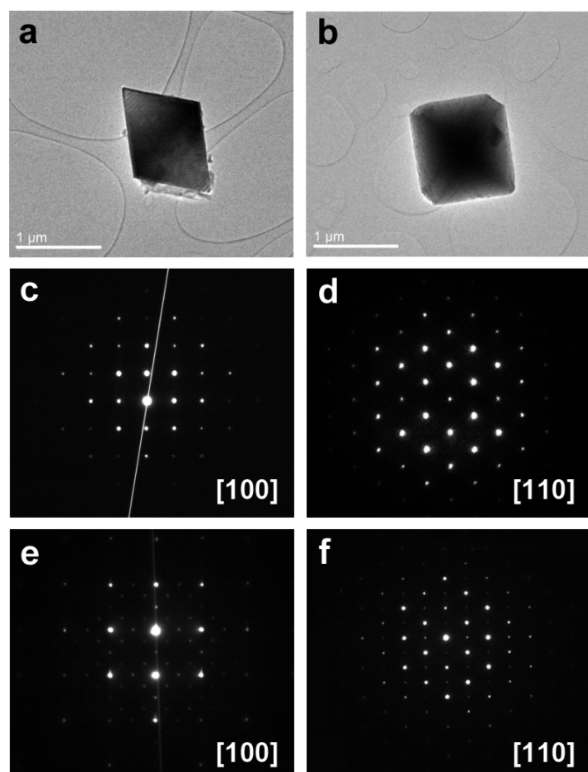


Figure 1. (a–b) TEM images of LNMO900 powder sample. Selected area electron diffraction patterns of (c–d) LNMO900 and (e–f) LNMO700-48 samples at zone axis of [100] and [110].

(SAED) patterns of the LNMO900 powder samples. The LNMO900 consisted of particles with octahedron-shaped morphology of which edges were typically $\sim 1 \mu\text{m}$ in length. Its SAED patterns at two different zone axes of [100] and [110] agree well with those of the typical cubic spinel structure with a space group (SG) of $Fd\bar{3}m$; where Ni and Mn are disordered in the $16d$ octahedral interstitials.⁵ The LNMO900 sample was annealed at 700 °C for 48 h in air (LNMO700-48), which has been known as a condition that promotes Ni and Mn ordering.^{5,8} Parts e and f of Figure 1 respectively are SAED patterns at [100] and [110] zone axes for the LNMO700-48 powder sample. Both e and f revealed additional spots (not seen in the LNMO900 sample), which originate from the ordering of Ni and Mn in the LNMO.⁵

As the large particle size ($\sim 1 \mu\text{m}$) hindered high resolution TEM (HR-TEM) imaging, the LNMO700-48 powder was

prepared as a thin-sliced specimen. Figure 2 shows the resulting TEM image of the cross-sectional area of the LNMO700-48

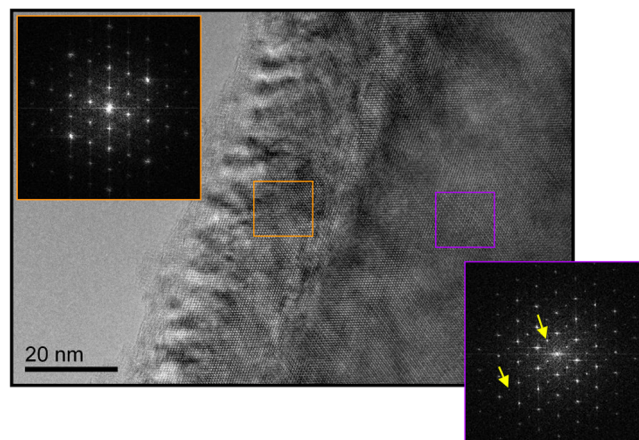


Figure 2. Cross-sectional high resolution TEM images and fast FFT patterns of two highlighted areas (orange nearby the surface and purple in bulk) based on [110] zone-axis. Yellow arrows indicate representative superlattice peaks with different intensities.

specimen from surface to bulk. The inset fast Fourier transform (FFT) pattern from the near surface bulk region (purple box) clearly shows the extra diffraction spots which indicates the existence of Ni/Mn ordering in the spinel structure. In contrast, such ordering spots were barely perceptible in the FFT pattern generated from the surface region (orange box), which indicates the absence of lattice ordering in this region.

As the fast Fourier transforms (FFT) are acquired from adjacent center and edge areas in the sample, double diffraction should not be the origin of the extra diffraction spots. It was also observed that the intensity of the extra diffraction spots (e.g., peaks marked with yellow arrows in Figure 2) varied from region to region in the grain bulk, which indicates that the crystal structure might not be fully (or homogeneously) ordered. In fact, the visible strain contrast of grains in Figure 2 (both on surface and grain bulk) further indicates such structural inhomogeneity at nanoscales.

This result agrees with the computational prediction by Lee and Persson,²⁶ where the surface energy of the ordered and disordered LNMO were calculated via the density functional theory for different facets and terminations. Their results suggested that even the well-ordered LNMO prefers to have locally deviated Ni/Mn distribution from the ideal $P4_332$ symmetry in the surface area, while the disordered LNMO retained the disordered Ni/Mn distribution over all parts of the material, both in the surface and bulk-inside. Their calculation data agree well with our experimental data. Considering that the SAED data in Figure 1 were collected for larger area of particles, it will be reasonable that the ordering peaks from the LNMO700-48 sample in Figure 1f only reflects the average ordering status.

To better recognize the local variation of order/disorder, a SAED pattern measured from the bulk of the thin-sliced specimen was processed to only show the extra peaks originating from the Ni/Mn ordering. Supporting Information (SI) Figure S1 shows a few nanometer-sized disordered domains (dark region) between the bright peaks from the ordered domains. This result clearly shows the existence of nanosized disordered domains in the bulk of the LNMO700-48

sample and suggests an intimate mixture of the ordered and disordered domains within each particle. As diffraction techniques provide average structural information and relatively sensitive to bulk (for this micron-sized particles), X-ray and neutron diffraction analyses were performed to quantify the ordered and disordered nanodomains.

X-ray and Neutron Diffraction of LNMO Spinel. The effect of annealing at 700 °C in air on the crystal structure of the LNMO was investigated by a joint refinement of XRD and neutron powder diffraction data. Figure 3 compares the powder

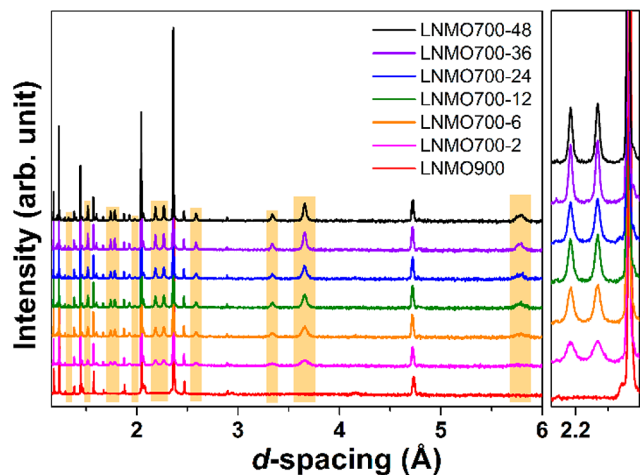


Figure 3. Evolution of powder neutron diffraction patterns of LNMO samples with 700 °C annealing time. Representative reflections associated with the Ni/Mn ordering were highlighted in orange. Right-hand side figure shows expanded view showing the growth of characteristic reflections with annealing time from ordered phase.

neutron diffraction data for various LNMO samples. Characteristic reflections that only belong to the ordered spinel phase (formed as a result of Ni/Mn ordering) were broader than the reflections that belong to both the ordered and disordered spinel domains. However, these characteristic reflections from ordered domains became narrower with annealing at 700 °C.

Based on the TEM data, two different structural models were employed to reflect the nanosized ordered domain embedded in the disordered LNMO spinel phase; (i) two-phase model with individual ordered and disordered LNMO phase and (ii) one-phase model only consisting of ordered LNMO domains where peak broadening was treated with microstructural effects. In the case of the one-phase model with ordered phase, the Mn/Ni are allowed to mix and have disordered to a large extent over the two sites. Therefore, they are in the ordered structure ($P4_332$), but with largely disordered cation occupancies. Recently, Rodríguez-Carvajal introduced a refinement method to improve the treatment for the broadening issue of Bragg reflections that stem from microstructural effects.²⁷ Using this modeling technique, various samples containing size broadening could be fitted using the Voigt approximation in the FullProf software.

The Rietveld refinement based on the two-phase model was performed using the GSAS software. SI Table S1 summarizes the results of the refinements. The LNMO900 sample consisted of 89.5% of disordered LNMO (SG: $Fd\bar{3}m$), 9.2% Ni_6MnO_8 , and 1.3% of $Mn_{0.95}Li_{0.05}O_2$. Either the Ni_6MnO_8 or the $Mn_{0.95}Li_{0.05}O_2$ rock-salt structures may be present depending upon the local cation distribution; these phases would form

as a result of migration of Li^+ , Ni^{2+} , and $Mn^{3+/4+}$ cations at temperatures above 700 °C.¹⁴ These secondary phases were selected after carefully examining possible candidates of various secondary phases. As a good example, LNMO900 sample showed impurity peak at a d -spacing of 4.76 Å, which was weak but visible in both X-ray and neutron diffraction. Given the fact that any possible binary oxides have much smaller lattice parameters (~ 4 Å) than 4.76 Å, Ni_6MnO_8 was selected from literatures^{11,28,29} and provided good fitting results. Though phases such as $Li_{1-x}Ni_xO$,⁷ $(Li_xMn_{0.66}Ni_{0.34})_yO$,⁶ and $LiMn_2O_4$ ^{7,30} have been suggested in literatures, the reported impurity phases in this study appeared to fit well with the data and are chemically reasonable; other impurities may be present in LNMO samples depending upon the sample preparation protocol. After annealing at 700 °C, however, the LNMO samples showed a trend of decreasing amount of secondary phase with increasing annealing time. For example, 2 h of annealing at 700 °C decreased the total amount of secondary phases from 10.5% (for LNMO900) to 3.8% (for LNMO700-2). Figure 4 shows the variation of phase fractions with

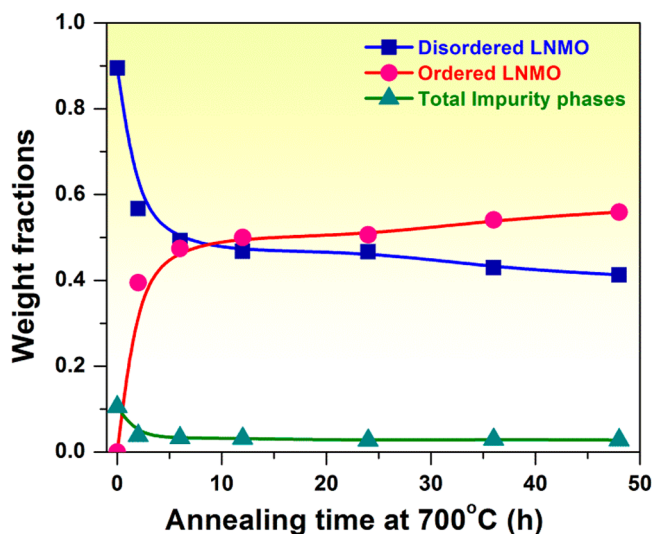


Figure 4. Variation of phase fractions with annealing times from Rietveld refinement data based on the two-phase structural model with mixed disordered/ordered LNMO phases.

annealing times. The phase fraction of ordered LNMO increased rapidly in the first 6 h of the dwelling period, followed by a much lower rate of increase thereafter. It is notable that the disordered LNMO phase fraction was $\sim 41\%$ after annealing at 700 °C for 48 h, which may support the qualitative TEM analysis results discussed in the previous section that indicated a mixture of order and disorder in the bulk (SI Figure S1).

Encouraged by the Rodríguez-Carvajal report, the Rietveld refinement based on the one-phase model was performed using the Fullprof software. All data were fitted based on the ordered LNMO phase (SG: $P4_332$), but with a rule that characteristic reflections from ordered spinel are broader than the reflections that contain contributions from both disordered and ordered domains. This model provides a description of the broader peaks originating from the short-range Ni/Mn ordered domains while accounting for the sharp reflections provided by underlying spinel lattice. The representative refinement profiles are illustrated in SI Figure S2. Table 2 lists the results of

Table 2. Refinement Data of Various LNMO Based on a Structure Model with a Single LNMO Phases

samples	LNMO900	LNMO700-2	LNMO700-6	LNMO700-12	LNMO700-24	LNMO700-36	LNMO700-48
Goodness of Fit							
R_{wp}	0.015	4.54	4.00	4.32	4.15	4.51	3.98
χ^2	5.90	8.56	7.22	7.75	6.79	9.27	6.67
Phase I: LNMO Disordered (SG: $Fd\bar{3}m$)		Phase I: LNMO Ordered Spinel (SG: $P4_32$)					
a (Å)	8.178	8.174	8.172	8.172	8.172	8.171	8.172
vol. (Å ³)	546.91(2)	546.15	545.64	545.77	545.65	545.56	545.75
wt. fraction	0.895(1)	0.953(31)	0.963(26)	0.963(27)	0.965(27)	0.964(28)	0.967(25)
Ni content	0.439	0.460(2)	0.473(2)	0.474(2)	0.485(2)	0.475(2)	0.478(2)
Mn content	1.561	1.540(2)	1.527(2)	1.526(2)	1.515(2)	1.525(2)	1.522(2)
oxidation state of Mn	3.92	3.95	3.96	3.97	3.98	3.97	3.97
Phase II: Ni _{0.95} MnO ₈ (SG: $Fm\bar{3}m$)		Phase II: Li _{0.4} Ni _{1.6} O ₂ (SG: $Fm\bar{3}m$)					
a (Å)	8.279	4.137	4.138(1)	4.135(1)	4.138(1)	4.133(1)	4.135(1)
vol. (Å ³)	567.5(1)	70.82	70.83	70.72	70.86	70.60	70.70
wt. fraction	0.092(2)	0.038(3)	0.030(2)	0.030(2)	0.029(2)	0.030(3)	0.027(2)
Phase III: Mn _{0.95} Li _{0.05} O ₂ (SG: $Fm\bar{3}m$)		Phase III: NiO (SG: $Fm\bar{3}m$)					
a (Å)	4.048(1)	4.113(1)	4.112(1)	4.113(1)	4.113(1)	4.110(1)	4.113(1)
vol. (Å ³)	66.32(4)	69.59	69.52	69.59	69.59	69.44	69.56
wt. fraction	0.013(2)	0.009(1)	0.007(1)	0.007(1)	0.006(1)	0.006(1)	0.006(1)

refinement, which show improved goodness of fit compared with the previous data based on mixed (disordered/ordered) LNMO phases (see SI Table S1). The improved fit suggests that the anisotropic description for peak broadening, as used in the single phase model, is likely required in the two phase model to achieve a similar quality of fit.

Shin et al.⁷ reported the presence of ordered Ni/Mn domains over short-ranges from the substituted spinels (LiNi_{1-x}M_xMn_{1.5}O₄, M = Cr, Fe, and Ga). Their neutron powder diffraction result suggested the existence of nanosized short-range ordered domains, but incorporation of dopant ions (i.e., Cr, Fe, and Ga) significantly limited the growth of ordered domains. Compared with the LiNi_{1-x}M_xMn_{1.5}O₄, the LNMO samples annealed at 700 °C showed more prominent ordering reflections with annealing time from 2 to 48 h. The sharpening of the characteristic reflections from the ordered spinel suggests that domain sizes of the short-range order are increasing with annealing time. The broad reflections from the ordered regions that are expected to be present under the sharper reflections (e.g., (222) and (400)) are not clearly evident, which suggests that there is very little change in atomic positions of the underlying AB₂O₄ lattice between the disordered and ordered regions. The width of the broader reflections is largely defined by the cation distribution, whereas the sharper reflections indicate that the underlying spinel lattice is highly crystalline. Unlike the broad reflections from the ordered phase, there are no peaks that uniquely correspond to the disordered regions. For this reason, a precise estimate of the size for disordered domains is not possible. Therefore, the sizes of ordered domains and the underlying spinel lattice (sharper reflections) were determined using Scherrer formula, with the assumption that domain size broadening is dominant over strain broadening in these samples. A total of 12 reflections were selected for calculating the domain size using the Scherrer formula: (444), (622), (331), (400), (222), (111) for spinel lattice (relatively sharp reflections) and (532), (433), (332), (310), (211), (110) for characteristic ordered reflections. Except the (111) reflection, full width at half maximum (FWHM) values of the reflections were very close to each other, especially for the characteristic ordered reflections (see SI Table S2). Therefore,

we took their median values as their representative domain sizes.

Figure 5 illustrates the resulting domain sizes of the spinel lattice-frame (sharper reflections) and the ordered phase at

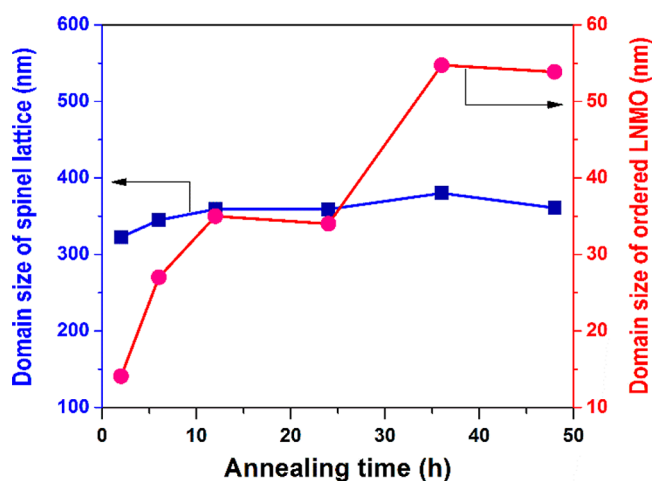


Figure 5. Variation in domain sizes of the underlying spinel lattice (left axis) and cation-ordered (right axis) LNMO regions calculated using the Scherrer formula.

different annealing times. The size of underlying spinel domains was relatively constant; it only increased from 323 nm (for 2 h) to 361 nm (for 48 h), which corresponds to 11.8% of increase. For the sharper reflections, sample broadening is suggested by the fact that they are broader than instrument resolution. The sharper reflections are closer to being resolution limited, making the size estimates less precise, and therefore mainly serve to suggest a relatively small change in domain size of the underlying lattice with time. However, the size of short-range ordered domains, which correspond to the Ni/Mn ordered LNMO, increased with annealing time from 14 nm (for 2 h) to 54 nm (for 48 h), which corresponds to 385% increase.

Table 2 shows that fractions of secondary phases decreased rapidly for the first 6 h during annealing at 700 °C, followed by a slower rate of decrease, but still showing 3.3% after 48 h.

During the annealing, the Ni and/or Mn present in the secondary phases can be incorporated into the parent LNMO phase, which makes the Ni and Mn content closer to the ideal $\text{LiNi}_{0.5}\text{Mn}_{1.5}\text{O}_4$ composition. Accordingly, the Mn oxidation state increased from 3.92 (for LNMO900) to 3.97 (for LNMO700-48) after annealing at 700 °C for 48 h. The oxidation of Mn ions led to decreases in lattice parameter (a) and unit cell volume.

Our data demonstrate that annealing at 700 °C decreases the content of rock-salt secondary phases with oxygen compensation in air (see SI Figure S3), and subsequently, incorporating Ni and/or Mn into the parent LNMO spinel phase produces a material that is close to having the ideal Ni/Mn ratio of 1/3, a condition that is necessary for successful Ni/Mn ordering.⁶ Although we tried to refine oxygen occupancies in spinel phases, we could not find reasonable amount of oxygen vacancies using either the two phases or the one phase model. It is assumed that relatively small oxygen-vacancy contents in spinel may make it less sensitive and challenging for the refinements.

FT-IR Analyses of LNMO Spinel. To determine the degree of bulk cation ordering in the LNMO material resulting from different times of annealing at 700 °C, FT-IR was employed. Infrared spectroscopy is a sensitive probe to the local structure of materials and has been demonstrated to be a useful tool to monitor the degree of Ni/Mn ordering in LNMO.^{31,32} Figure 6 shows the FT-IR absorbance spectra for a series of LNMO for different annealing times at 700 °C.

The LNMO900 starting material, obtained from the initial synthesis heating at 900 °C, exhibits an FT-IR spectrum that is in accordance with that reported for disordered ($Fd\bar{3}m$) LNMO.^{31,33} The spectrum of the disordered species consists

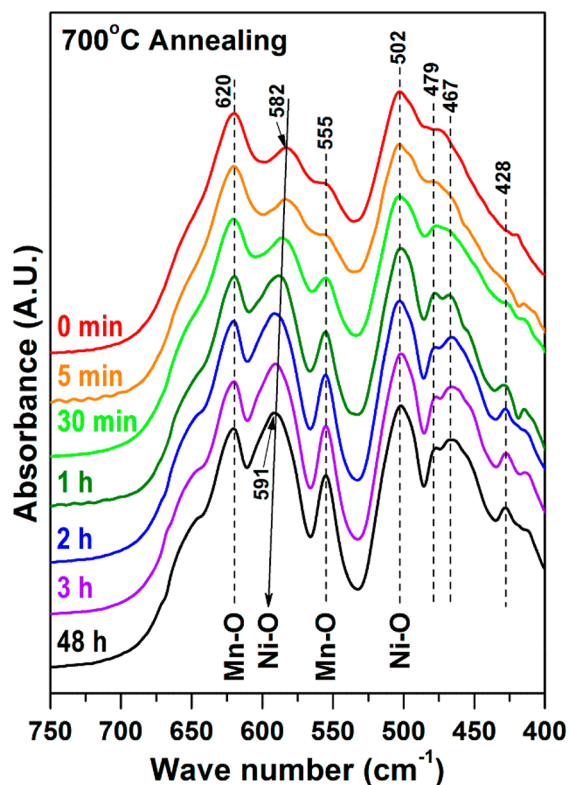


Figure 6. FT-IR spectra of various LNMO powder samples after annealing at 700 °C for different dwelling times.

of several broad and ill-defined bands that can be mainly attributed to vibrations associated with Mn–O and Ni–O bonds. Upon annealing for 30 min, features that are signatures of the ordered ($P4_332$) phase, particularly the appearance of defined peaks at 428, 467, and 555 cm^{-1} and a general decrease in peak bandwidths, can be seen. The increase in distinguishable peaks is the result of a reduction of space symmetry from disordered to ordered phase resulting in the increase in IR active bands. Thus, after only 30 min, both phases are present in the sample. After 1 h annealing, the recorded FT-IR spectra are dominated by peaks of the ordered phase with little measurable contribution from the disordered phase.

Our TEM, powder diffraction, and FT-IR data demonstrate the evolution of ordered LNMO crystalline with annealing time at 700 °C. For the LNMO synthesized by the solid-state reaction method, the degree of ordering became stabilized after annealing at 700 °C for 6 h, accompanied by decreasing amount of secondary phases. The annealing longer than 6 h led to the growth of ordered domains with slow increase in the degree of ordering. As the result, the LNMO700-48 sample still consists of mixture of order/disorder nanodomains.

Effect of Disorder/Ordering on the Electrochemical Properties of LNMO Spinel. Based on these structural characterizations, the effect of ordering behavior on the electrochemical properties of LNMO was investigated. Figure 7 compares voltage profiles of the various LNMO/Li half-cells.

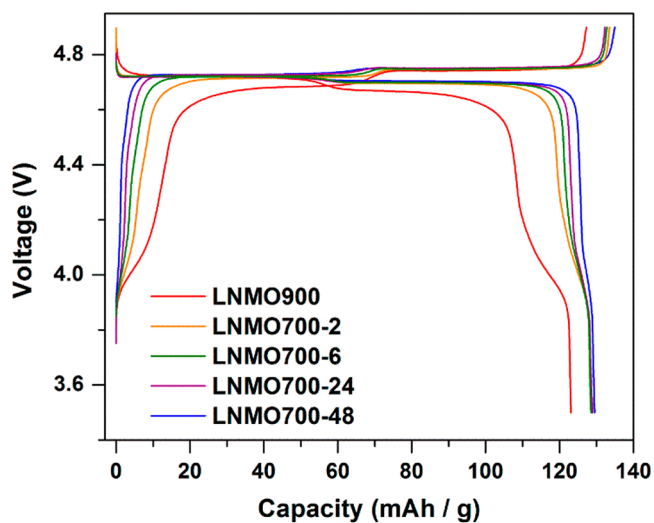


Figure 7. Comparison of voltage profiles of the various LNMO samples obtained using coin half-cells; recorded at 3rd cycle with C/10-rate at 30 °C.

The LNMO900 sample delivered a specific discharge capacity of ca. 123 mAh/g, including ~15 mAh/g of capacity from the $\text{Mn}^{3+/4+}$ redox at around 4 V. With increasing annealing time at 700 °C, the LNMO samples showed a trend of increasing capacity from the slope at ~4.75 V ($\text{Ni}^{2+/4+}$ redox) and decreasing capacity from the ~4 V region ($\text{Mn}^{3+/4+}$ redox), while maintaining ~130 mAh/g of discharge capacity. The capacity increase in LNMO after annealing at 700 °C (compared with that of LNMO900) can be explained by its lower amount of secondary phases, the impurities being electrochemically inactive. For example, structural refinement data (see Table 2) revealed that the amount of secondary phases rapidly decreased from 10.5% (for LNMO900 sample) to 4.7% after annealing at 700 °C for 2 h. Further increase in

annealing time (6, 24, and 48 h) at 700 °C only showed a slight capacity increase because of a minor decrease in the amount of secondary phases from 4.7% (for LNMO700-2 sample) to 3.5% after 48 h annealing.

Figure 8 compares the dQ/dV profiles of the various LNMO positive electrode materials prepared before and after annealing

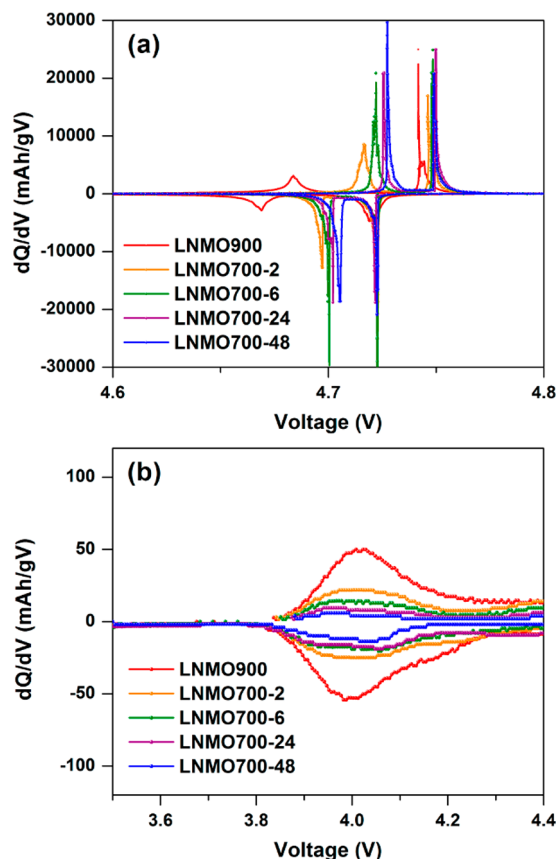


Figure 8. Comparison of differential capacity (dQ/dV) profiles of the various LNMO samples obtained using coin half-cells; (a) in the voltage range 4.6–4.8 V and (b) in the voltage range 3.5–4.4 V recorded at the 3rd cycle with C/10-rate at 30 °C.

at 700 °C. In Figure 8b, a decrease in the area of ~4 V peak with increasing annealing time (0–48 h) at 700 °C is attributed to an increase in average oxidation states of Mn ions in the LNMO samples. The presence of Mn³⁺ in LNMO can be explained by (i) deviation of chemical composition due to the

formation of secondary phases as shown in Table 2 and (ii) oxygen vacancies in LNMO generated during high temperature (900 °C) sintering. Both mechanisms may contribute to the formation of Mn³⁺ in LNMO. SI Table S3 shows that electrochemical data are well supported with structural analysis data. For example, the ratio of Ni^{2+/4+} and Mn^{3+/4+} redox capacities agrees very well with the chemical compositions determined by the Rietveld refinement (see Table 2).

The dQ/dV profiles show some of the interesting impacts that order/disorder nanodomains have on the electrochemical properties of LNMO. Table 3 summarizes the two Ni redox positions and the voltage gaps between them as determined from the dQ/dV profiles. The first redox peak, which has been assumed to originate from the Ni^{2+/3+} redox, is shifted toward higher voltages with increasing annealing time at 700 °C. For instance, the first Ni^{2+/3+} redox peak position increased ~40 mV from LNMO900 to LNMO700-48. The second Ni redox peak position, which has been assumed to originate from the Ni^{3+/4+} redox, was relatively stable with negligible amount of voltage increase with annealing time. If one assumes a simple physical mixture of disordered and ordered spinels, each spinel phase would deliver individual Ni^{2+/4+} redox peaks at their own distinct voltages. In contrast, Figure 8a shows smooth increase in the redox voltage with annealing time at 700 °C. This result suggests that the order/disorder nanodomains are integrated and deliver an average redox voltage, which potentially depends on the degree of ordering in the spinel lattices.

The open circuit voltages (OCV) of the LNMO electrodes were measured at various SOC to eliminate the influence of IR increase/drop on the dQ/dV profiles of the cells. Figure 9 plotted OCVs of the various LNMO electrodes. The first Ni^{2+/3+} redox voltages stiffly increased with annealing time at 700 °C (marked with arrow). In contrast, increase of the second Ni^{3+/4+} redox voltages were relatively small and became similar each other after 2 h annealing at 700 °C (ca. 4.734 V). The OCV values were differentiated to determine peak positions for the first and second Ni redox. The results are listed in Table 3. These average OCV values are comparable with median redox voltages between charge and discharge from the dQ/dV profiles. This result again shows that evolution of ordered nanodomains increases the overall OCVs of the LNMO electrodes.

The measured dQ/dV and OCV profiles agree well with the previous computational work by Lee and Persson,^{19,20} in which the energy and voltage profiles of the P₄₃₂ ordered and the random disordered LNMO were obtained using the density functional theory calculations. According to their result, the

Table 3. Effect of Annealing Time on the Ni^{2+/4+} Redox Peak Positions, the Deviations Between Two Redox Peaks, and the Capacity Retention of LNMO/Li Half-Cells^a

samples	charging (from dQ/dV plots)			discharging (from dQ/dV plots)			avg. OCVs (from OCV plots)			capacity retention (%) ^b
	1st Ni redox (V)	2nd Ni redox (V)	deviation (mV)	1st Ni redox (V)	2nd Ni redox (V)	deviation (mV)	1st Ni redox (V)	2nd Ni redox (V)	deviation (mV)	
LNMO900	4.684	4.742	58	4.669	4.719	50	4.677	4.728	51	92.9
LNMO700-2	4.717	4.747	30	4.697	4.723	26	4.706	4.733	27	92.3
LNMO700-6	4.722	4.749	27	4.700	4.722	22	4.71	4.733	23	90.0
LNMO700-24	4.725	4.750	25	4.702	4.722	20	4.713	4.734	21	86.0
LNMO700-48	4.727	4.749	22	4.705	4.723	18	4.716	4.735	19	82.1

^aThe peak voltages from dQ/dV plots (Figure 8) on charge/discharge and average OCV values from OCV plots (Figure 9) are compared. ^bCapacity retention after 100 cycles with a C/10-rate at 30 °C.

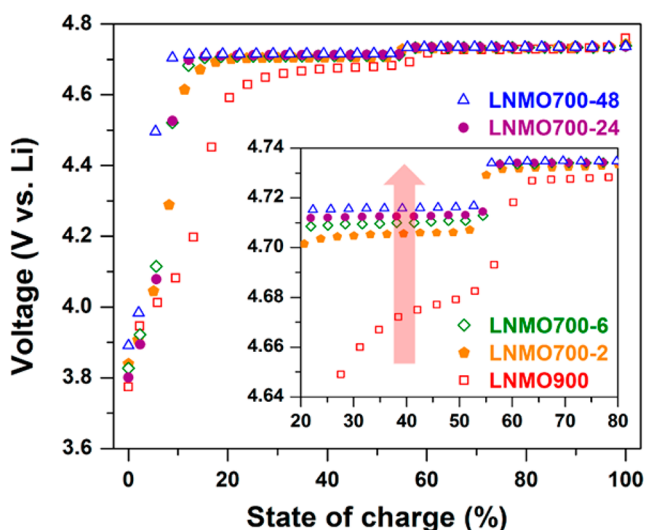


Figure 9. Open circuit voltage (OCV) profiles of various LNMO samples. Inset is a magnification of the OCV profiles in a range of 4.64–4.74 V and 20–80% SOC. These data were collected after three formation cycles.

predicted voltage profile of the ordered LNMO is a constant voltage plateau originated from a two-phase reaction in overall Li content (i.e., $x = 0-1$ in $\text{Li}_{1-x}\text{Ni}_{0.5}\text{Mn}_{1.5}\text{O}_4$). In contrast, the disordered LNMO showed two redox reactions: $\text{Ni}^{3+/4+}$ between 50 and 100% SOC and $\text{Ni}^{2+/3+}$ between 0 and 50% SOC. The computed $\text{Ni}^{3+/4+}$ redox voltage in the disordered LNMO was similar to the $\text{Ni}^{2+/4+}$ redox voltage in the ideally ordered LNMO, while the computed $\text{Ni}^{2+/3+}$ redox voltage in the disordered LNMO was lower than two others by 50–90 mV depending on the degree of disordering. This result implies that the $\text{Ni}^{2+/3+}$ redox voltage will shift to the $\text{Ni}^{3+/4+}$ (and the $\text{Ni}^{2+/4+}$ in the ideally ordered LNMO) redox voltage when the disordered LNMO transforms to the ordered LNMO through the annealing, which agrees well with our experimental result. As it was also suggested that the voltage profile of the ordered LNMO should be a single plateau in the 0–100% SOC windows, any voltage steps observed would infer the existence of local disorder. In other words, the distinct $\text{Ni}^{2+/3+}$ redox (indicated as the first Ni redox in Table 3) peak observed from the dQ/dV profile is attributed to the substantial fraction of the disordered LNMO as explained in earlier section.

SI Figure S4 compares the cycle lives of half-cells using the various LNMO positive electrode materials prepared before and after annealing at 700 °C. The LNMO900 electrode delivered good capacity retention ($\sim 95\%$ after 100 cycles) but showed the lowest initial capacity (~ 120 mAh/g) due to the large quantity of secondary phases (10.5%). Although 700 °C annealed LNMO samples delivered higher initial capacity of ~ 130 mAh/g, their cycle lives degraded with increasing annealing time (see Table 3), which agrees well with some literature data.^{14,16}

Figure 10 compares voltage profiles of the various LNMO samples under various current densities in half-cells. The thicknesses of positive electrodes were maintained to be ~ 40 μm , containing ~ 5 mg/cm² of LNMO powders. At a given current density, the discharge capacity and the cell voltage increase from LNMO900 to LNMO700-2. This can be explained by the rapid decrease in the amount of secondary phase after annealing at 700 °C for 2 h and the secondary

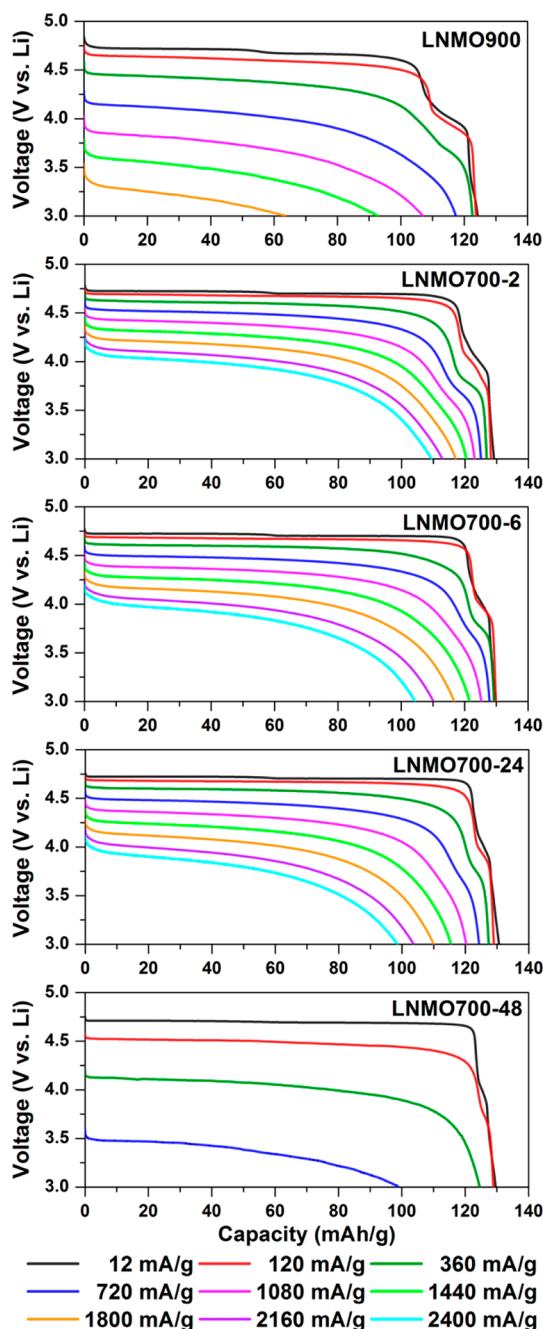


Figure 10. Voltage profiles of LNMO/Li half-cells under various current densities at 30 °C. The cells were charged with a constant rate of $C/7$ followed by discharging with various current densities ranging from 12 mA/g ($\sim C/10$ -rate) to 2400 mA/g (~ 20 C-rate) (see legend).

phases present at grain boundaries or surfaces of spinel particles,⁶ which would impede the Li^+ ion and/or electron conduction. Further annealing longer than 2 h, however, deteriorated the rate capability of the LNMO. For example, the rate performance degraded rapidly from LNMO700-24 to LNMO700-48, as shown in Figure 11. In particular, the LNMO700-48 delivered a poor rate performance with low cell voltage, which agree well with the literature data.^{5,34,35} Yang et al.³⁵ demonstrated that disordered LNMO powders delivers better rate-capability than ordered LNMO in both micron- and nanosized primary particles. The inferior rate capability of the

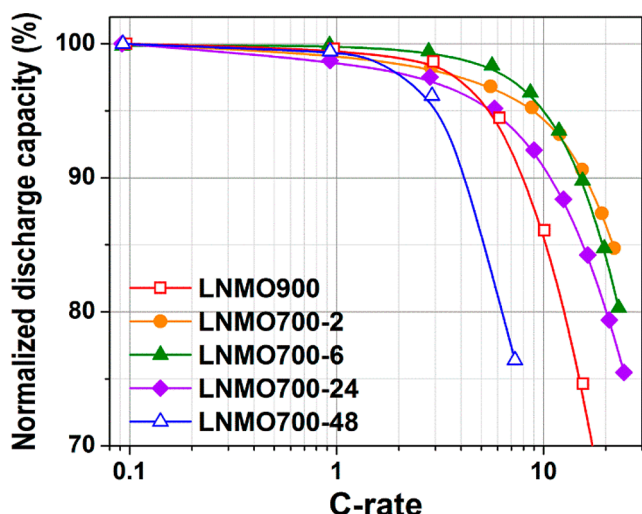


Figure 11. Comparison of C-rate performances of LNMO with different annealing times. The discharge capacities of LNMO/Li half-cells were normalized based on discharge capacities at $\sim C/10$ -rate.

ordered LNMO to that of the disordered LNMO has been explained by (i) strain associated with additional phase transition⁵ and (ii) lower ionic^{17,34} and electronic⁹ conductivities of the ordered LNMO. As shown in Figure 10, the increasing voltage IR drop (lowering cell voltage) from LNMO700-2 to LNMO700-48 manifests the increasing impedance of LNMO with annealing time. These results suggest that the increase in the degree of ordering (or size of ordered domain) is responsible for the deterioration of rate performance of the LNMO half-cells.

Our results demonstrated that the degree of ordering impacts the electrochemical properties of the LNMO. The increase in OCV with the degree of ordering in LNMO can be explained by variations of phase diagrams depending on the degree of disordering, following recently calculated results.^{19,20} Among the various samples investigated, the LNMO delivered optimal battery performances (capacity, cycle life, and rate capability) after annealing at 700 °C for 2 h. This sample showed the respective advantages from both disordered and ordered spinel regions: better spinel-phase purity (thus, higher initial capacity) from the ordered LNMO component and better cycle life and rate capability from the disordered LNMO component.

CONCLUSION

In this work, we systematically controlled the evolution of Ni and Mn ordering in LNMO samples to optimize its battery performance.

- (1) TEM analysis revealed that LNMO has nanodomains of Ni/Mn disordered and ordered phases after annealing at 700 °C for 48 h, which has been reported as the optimal condition to prepare the ordered LNMO phase.
- (2) Structural characterization using X-ray and neutron diffraction techniques showed that the size of Ni/Mn ordered domains in LNMO increased with annealing time at 700 °C. The amount of secondary phases in LNMO decreased rapidly from 10.5% (before annealing) to 4.7% after annealing for 2 h.
- (3) FT-IR spectroscopy showed that Ni/Mn ordering was noticeable after annealing at 700 °C for 30 min and became dominant after 1 h.

- (4) The gravimetric capacity of LNMO increased from 123 to 130 mAh/g after annealing at 700 °C because of the decrease in secondary phase contents.
- (5) Cycle lives of the LNMO half-cells degraded with increasing annealing time from 92.9% (before annealing) to 82.1% (48 h annealing) after 100 cycles with a C/5-rate at 30 °C. In addition, the LNMO demonstrated lower rate capability after annealing at 700 °C for 48 h.
- (6) The LNMO delivered optimal battery performances (capacity, cycle life, and rate capability) after annealing at 700 °C for 2 h. This sample showed the respective advantages from both disordered and ordered spinels; better spinel-phase purity (thus, higher initial capacity) from the ordered LNMO and better cycle life and rate capability from the disordered LNMO.

ASSOCIATED CONTENT

Supporting Information

Structural analysis, thermogravimetric analysis, and cycling data. This material is available free of charge via the Internet at <http://pubs.acs.org>.

AUTHOR INFORMATION

Corresponding Author

*Email: junghyun.kim@gm.com.

Notes

The authors declare no competing financial interest.

ACKNOWLEDGMENTS

The authors to thank Mark W. Verbrugge of the Chemical and Materials Systems Laboratory in GM R&D for many helpful discussions. The TEM and neutron diffraction studies were performed through user projects (through Center for Naonphase Materials Sciences for TEM and Spallation Neutron Source for neutron diffraction) supported by the Scientific User Facilities Division and Materials Sciences and Engineering Division, Office of Basic Energy Sciences, U.S. Department of Energy.

REFERENCES

- (1) Kim, J.-H.; Pieczonka, N. P. W.; Yang, L. *ChemPhysChem* **2014**, DOI: 10.1002/cphc.201400052.
- (2) Manthiram, A.; Chemelewski, K.; Lee, E.-S. *Energy Environ. Sci.* **2014**, *7*, 1339–1350.
- (3) Julien, C. M.; Mauger, A. *Ionics* **2013**, *19*, 951–988.
- (4) Goodenough, J. B.; Kim, Y. *Chem. Mater.* **2010**, *22*, 587–603.
- (5) Kim, J.-H.; Myung, S.-T.; Yoon, C. S.; Kang, S. G.; Sun, Y.-K. *Chem. Mater.* **2004**, *16*, 906–914.
- (6) Cabana, J.; Casas-Cabanas, M.; Omenya, F. O.; Chernova, N. A.; Zeng, D.; Whittingham, M. S.; Grey, C. P. *Chem. Mater.* **2012**, *24*, 2952–2964.
- (7) Shin, D. W.; Bridges, C. A.; Huq, A.; Paranthaman, M. P.; Manthiram, A. *Chem. Mater.* **2012**, *24*, 3720–3731.
- (8) Ariyoshi, K.; Iwakoshi, Y.; Nakayama, N.; Ohzuku, T. *J. Electrochem. Soc.* **2004**, *151*, A296–A303.
- (9) Kunduraci, M.; Al-Sharab, J. F.; Amatucci, G. G. *Chem. Mater.* **2006**, *18*, 3585–3592.
- (10) Kunduraci, M.; Amatucci, G. G. *J. Power Sources* **2007**, *165*, 359–367.
- (11) Duncan, H.; Duguay, D.; Abu-Lebdeh, Y.; Davidson, I. J. *J. Electrochem. Soc.* **2011**, *158*, A537–A545.
- (12) Kim, J.-H.; Myung, S.-T.; Sun, Y.-K. *Electrochim. Acta* **2004**, *49*, 219–227.

- (13) Akimoto, J.; Takahashi, Y.; Gotoh, Y.; Kawaguchi, K.; Dokko, K.; Uchida, I. *Chem. Mater.* **2003**, *15*, 2984–2990.
- (14) Song, J.; Shin, D. W.; Lu, Y.; Amos, C. D.; Manthiram, A.; Goodenough, J. B. *Chem. Mater.* **2012**, *24*, 3101–3109.
- (15) Kim, J.-H.; Yoon, C. S.; Myung, S.-T.; Prakash, J.; Sun, Y.-K. *Electrochem. Solid-State Lett.* **2004**, *7*, A216.
- (16) Zheng, J.; Xiao, J.; Yu, X.; Kovarik, L.; Gu, M.; Omenya, F.; Chen, X.; Yang, X.-Q.; Liu, J.; Graff, G. L.; Whittingham, M. S.; Zhang, J.-G. *Phys. Chem. Chem. Phys.* **2012**, *14*, 13515–13521.
- (17) Kim, J.-H.; Myung, S.-T.; Yoon, C. S.; Oh, I.-H.; Sun, Y.-K. *J. Electrochem. Soc.* **2004**, *151*, A1911–A1918.
- (18) Ma, X.; Kang, B.; Ceder, G. *J. Electrochem. Soc.* **2010**, *157*, A925.
- (19) Lee, E.; Persson, K. A. *Chem. Mater.* **2013**, *25*, 2885–2889.
- (20) Lee, E.; Persson, K. A. *Energy Environ. Sci.* **2012**, *5*, 6047–6051.
- (21) Sushko, P. V.; Rosso, K. M.; Zhang, J.-G.; Liu, J.; Sushko, M. L. *Adv. Funct. Mater.* **2013**, 1–6.
- (22) Xia, H.; Meng, Y. S.; Lu, L.; Ceder, G. *J. Electrochem. Soc.* **2007**, *154*, A737–A743.
- (23) Larson, A. C.; Von Dreele, R. B. *Los Alamos Natl. Lab. Report LAUR 86-748*; Los Alamos National Laboratory: Los Alamos, NM1994.
- (24) Toby, B. H. *J. Appl. Crystallogr.* **2001**, *34*, 210–213.
- (25) Rodríguez-Carvajal, J. *Phys. B Condens. Matter* **1993**, *192*, 55–69.
- (26) Lee, E.; Persson, K. A. *Nanotechnology* **2013**, *24*, 424007.
- (27) Rodríguez-Carvajal, J. *Study of Microstructural Effects by Powder Diffraction Using the Program FULLPROF*; Laboratoire Léon Brillouin (CEA-CNRS): Gif-sur-Yvette, France, 2003.
- (28) Lee, E.-S.; Huq, A.; Chang, H.-Y.; Manthiram, A. *Chem. Mater.* **2012**, *24*, 600–612.
- (29) Taguchi, H.; Omori, S.; Nagao, M. *J. Solid State Chem.* **1995**, *118*, 112–116.
- (30) Mukai, K.; Ikedo, Y.; Kamazawa, K.; Brewer, J. H.; Ansaldo, E. J.; Chow, K. H.; Månsson, M.; Sugiyama, J. *RSC Adv.* **2013**, *3*, 11634.
- (31) Amdouni, N.; Zaghbi, K.; Gendron, F.; Mauger, A.; Julien, C. M. *Ionic* **2006**, *12*, 117–126.
- (32) Ivanova, S.; Zhecheva, E.; Stoyanova, R.; Nihtianova, D.; Wegner, S.; Tzvetkova, P.; Simova, S. *J. Phys. Chem. C* **2011**, *115*, 25170–25182.
- (33) Kunduraci, M.; Amatucci, G. G. *J. Electrochem. Soc.* **2006**, *153*, A1345–A1352.
- (34) Kunduraci, M.; Amatucci, G. G. *Electrochim. Acta* **2008**, *53*, 4193–4199.
- (35) Yang, J.; Han, X.; Zhang, X.; Cheng, F.; Chen, J. *Nano Res.* **2013**, *6*, 679–687.